Vol. 8 • No. 2 • January 24 • 2023

www.advmattechnol.com

ADVANCED MATERIALS TECHNOLOGIES

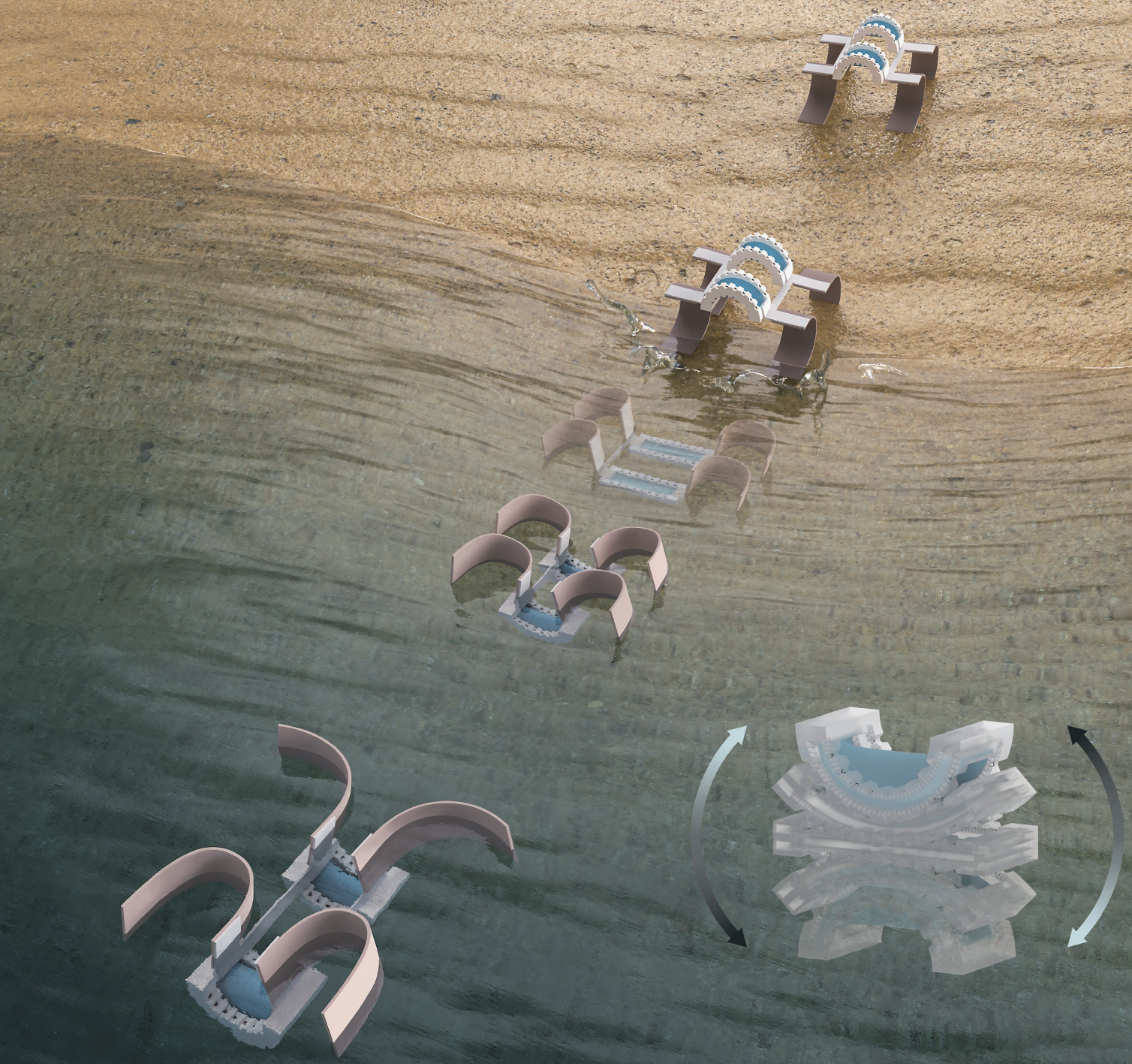

WILEY VCH

ADVANCED MATERIALS TECHNOLOGIES
www.advmattechnol.de

Highly Dynamic Bistable Soft Actuator for Reconfigurable Multimodal Soft Robots

Dinesh K. Patel, Xiaonan Huang, Yichi Luo, Mrunmayi Mungekar, M. Khalid Jawed, Lining Yao, and Carmel Majidi**

Matching the rich multimodality of natural organisms, i.e., the ability to transition between crawling and swimming, walking and jumping, etc., represents a grand challenge in the fields of soft and bio-inspired robotics. Here, a multimodal soft robot locomotion using highly compact and dynamic bistable soft actuators is achieved. These actuators are composed of a prestretched membrane sandwiched between two 3D printed frames with embedded shape memory alloy (SMA) coils. The actuator can swiftly transform between two oppositely curved states and generate a force of 0.3 N through a snap-through instability that is triggered after 0.2 s of electrical activation with an input power of 21.1 ± 0.32 *W* (i.e., electrical energy input of 4.22 ± 0.06 *J*. The consistency and robustness of the snap-through actuator response is experimentally validated through cyclical testing (580 cycles). The compact and fast-responding properties of the soft bistable actuator allow it to be used as an artificial muscle for shape-reconfigurable soft robots capable of multiple modes of SMA-powered locomotion. This is demonstrated by creating three soft robots, including a reconfigurable amphibious robot that can walk on land and swim in water, a jumping robot (multimodal crawler) that can crawl and jump, and a caterpillar-inspired rolling robot that can crawl and roll.

1. Introduction

In order to survive in the natural world, many animals have evolved to perform more than one mode of locomotion. For instance, besides crawling, some caterpillars are capable of rapidly curling themselves and rolling away to evade predators.[1] Crocodiles can both run on land and swim in the water in order to hunt their prey. Geese are capable of both flying for migration and walking to lay eggs in a nest. Inspired by nature, roboticists have developed machines capable of multimodal locomotion that are able to maneuver in unstructured environments for the application like search and rescue operation,[2] monitoring and defence.[3] Such multimodality is typically achieved through either i) shape morphing of the body, ii) gait change, or iii) using different mechanisms of actuation or propulsion. A popular approach is to use distinct propulsive mechanisms that are specialized for locomotion within a corresponding environment (e.g., propeller for flying and swimming and a wheel for locomotion on land[4,5]). However, multiple propulsive mechanisms can complicate design and add extra weight to such systems. Likewise, using a single propulsive mechanism capable of achieving distinct gaits and locomotion modes can simplify the design but often results in more limited mobility within certain environments.[6–8] A promising alternative is to utilize reversible shape morphing of the body, so that a common set of actuators or robotic limbs can be re-oriented to perform new modes of ground contact or fluid-structure interactions (see Refs. [9–11] for examples).

Soft robots are especially well-suited for reversible shape change due to their mechanical deformability and morphological response in response to controlled stimuli. Recently, Baines et al. proposed a shape morphing limb that can transform between a flipper and a leg by taking advantage of stiffness tuning.[12] The limb is implemented on a turtle-inspired robot[6] to facilitate amphibious locomotion. Shah et al. presented a

D. K. Patel, L. Yao
Human-Computer Interaction Institute
Morphing Matter Lab
School of Computer Science
Carnegie Mellon University
Pittsburgh, PA 15213, USA
E-mail: liningy@andrew.cmu.edu

The ORCID identification number(s) for the author(s) of this article can be found under https://doi.org/10.1002/admt.202201259.

DOI: 10.1002/admt.202201259

X. Huang, Y. Luo, C. Majidi
Department of Mechanical Engineering
Soft Machines Lab
Carnegie Mellon University
Pittsburgh, PA 15213, USA
E-mail: cmajidi@andrew.cmu.edu

M. Mungekar, M. K. Jawed
Department of Mechanical & Aerospace Engineering
University of California
Los Angeles, CA 90095, USA

C. Majidi
The Robotics Institute
Carnegie Mellon University
Pittsburgh, PA 15213, USA

shape morphing robot that can switch between a crawling gait and a rolling gait to adapt to different environments through the actuation of both internal and external bladders.[13] Although the transformation process is expensive in both energy (72 W) and time (16 min)[12] or relies on external bulky hardware,[13] these two studies provide a promising approach for designing robots that are capable of multi-modal locomotion through the use of reversible shape change.

Soft actuators capable of bistable configurations represent a promising solution to overcome the existing challenges with shape-reconfigurable soft robotic systems. Such actuators can take advantage of snap-through instabilities to achieve fast and reversible shape change through short impulses of stimulation. Moreover, they can maintain different stable shapes without continuously consuming energy.[14,15] In recent years, bistability has been exploited to create soft actuators for high-speed locomotion of soft robots,[16–18] fast grasping of soft grippers,[19–22] control of soft valves,[23–25] and construction of 3D reconfigurable electronics.[26,27] However, the potential benefit of using bistability to facilitate multi-modal and amphibious locomotion remains unexplored. Additionally, the majority of the aforementioned soft actuators still require relatively bulky hardware for power and control.

Here, we present a highly dynamic and compact soft actuator that uses a snap-through instability to swiftly switch between two oppositely curved states (**Figure 1**A–C). The bistable actuator is powered through thermal activation of embedded shape memory alloy (SMA) coils and is capable of achieving a snap-through transition within 0.2 and 0.3 s in air and water, respectively, when powered at 11.1 V (DC Power Supply, Eventek or battery). SMA is adopted here due to its fast response, high mass-to-weight ratio, and compatibility with small and lightweight electronics for power and control.[28–30] By harnessing the fast and reversible response that is achieved through snap-through instability, a pair of bistable soft actuators are implemented on an amphibious robot that is capable of rapid transitions between a swimming-favored state and a walking-favored state (Figure 1D). Inspired by the caterpillar, we also demonstrate that multiple bistable actuators can connected in series to create a soft robot that is capable of adapting to various ground terrain by swiftly transitioning between a crawling gait and a rolling gait (Figure 1E). Moreover, we perform a series of experimental measurements to characterize the bending response, blocking force, and cyclical repeatibility of the actuator. In addition, we develop an experimentally-validated analytic model and numerical simulation to examine the design principles of the actuator. These experimental and theoretical studies provide a framework for understanding the mechanics of the snap-through instability and the influence of design parameters on actuator performance.

2. Results

2.1. Design Overview

The bistable actuator is composed of two 3D printed elastomeric frames (epoxy aliphatic acrylate-polyurethane acrylate based elastomer) with embedded shape memory alloy coils (Dynalloy, wire diameter = 0.203 mm, outer diameter = 1.37 mm; Austenite

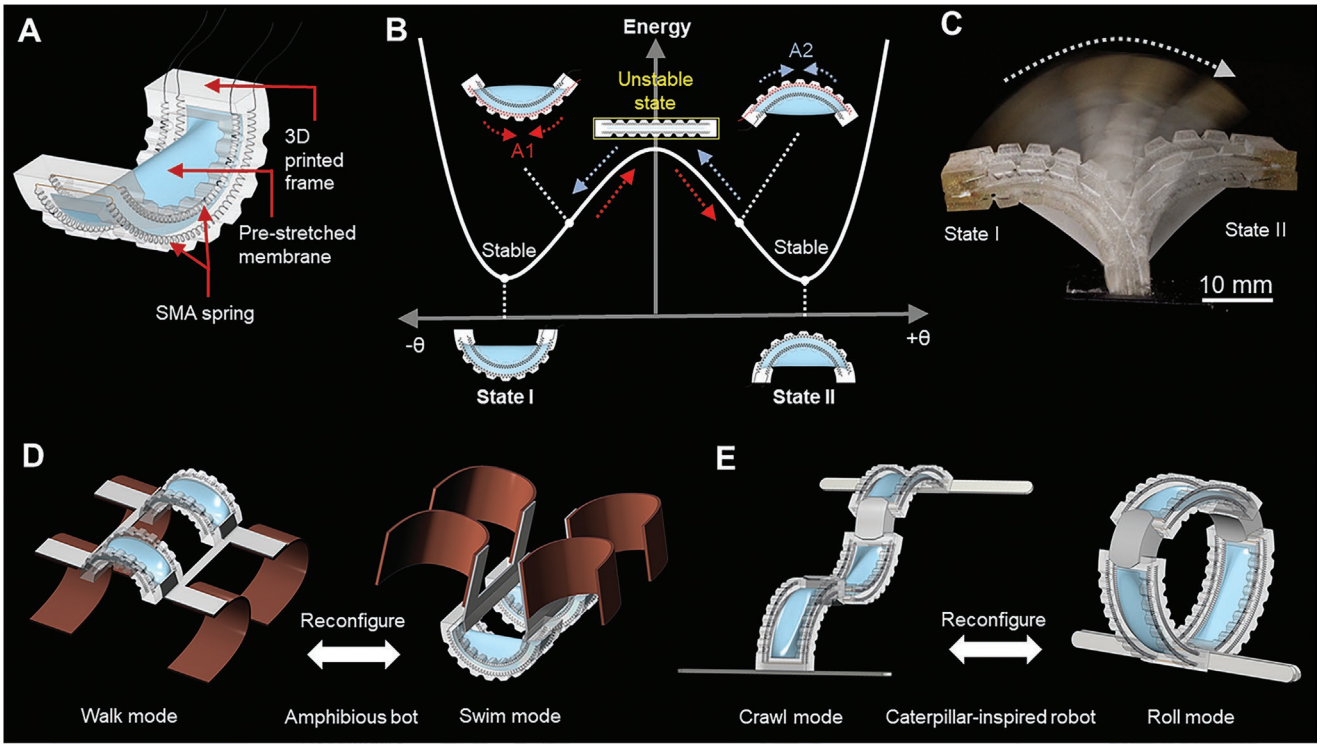

Figure 1. A) Schematic view of bistable actuator, B) Transition of bistable actuator from State I to State II and vice-versa with respect to free energy, C) Picture of bistable actuator triggered from state I to state II, Schematic (Rendering image) of reconfigurable multimodal and amphibious soft robots: D) a Amphibious bot and E) a Caterpillar-inspired robot.

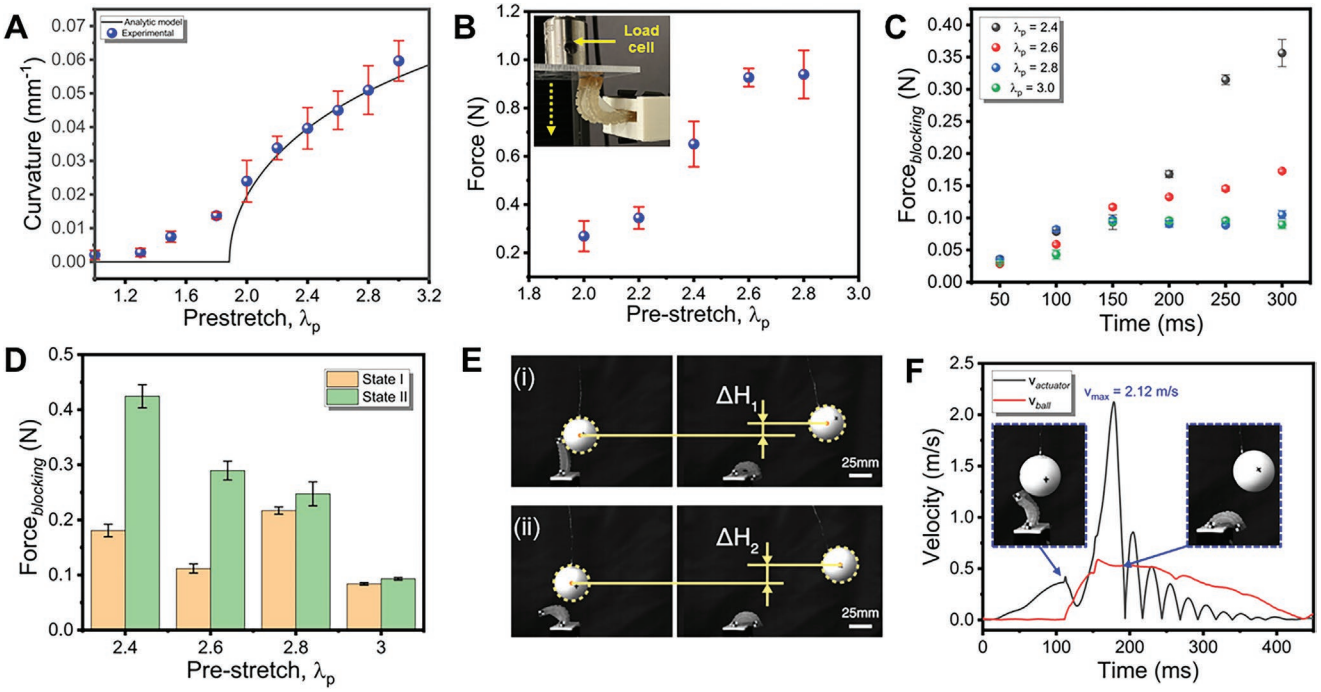

Figure 2. Characterization of the bistable actuator. A) Initial curavture for experimental and analytic model, B) Transition force (inset shows setup for transition force), C) Active force under different activation time from 50 to 300 ms as electrical input and D) Blocking force for bistable actuator on each state with different prestretch (λ_p) ranging from 2.4 to 3.0, E) A bistable actuator hits the ping pong ball with (i) 1.0 and (ii) 2.8 prestretch and F) Velocity change for bistable actuator (with prestretch (λ_p) = 2.8) and ping-pong ball.

finish temperature = 90 °C) and a prestretched membrane (4905 VHB tape, 3M) sandwiched between them. Frames are designed with ridges and holes to reduce their bending stiffness (Figure 1A). The actuator has two oppositely curved stable states (State I and II) as shown in Figure 1B. The natural curvature is generated from the prestretched membrane, which contributes to an internal residual stress and a double-well elastic potential energy profile. Details of the fabrication can be found in Experimental Section and Figure S1 (Supporting Information).

The actuator can swiftly tranform from one state to the other by activating the embedded SMA coil on the opposite side (Figure 1B,C; Movie S1, Supporting Information). For example, as the actuator I (A1) is activated (depicted by red arrows), contraction causes the structure to bend from State I toward State II. Once the input energy surpasses the local maximum potential energy of the structure, the structure snaps through the unstable state and bends downward. The actuator stays in State II even after the energy input is removed. Similarly, the actuator can swiftly transform back to State I by activating actuator II (A2) (again by a snap-through instability) after a cooling period of 10 s. We also perform a maximum frequency test under which the bistable actuator transforms swiftly at 1 Hz under a condition without exterior loading (t_a = 0.1 s and t_c = 0.9 s) for 100 times actuation or 50 cycles (Movie S2, Supporting information).

2.2. Membrane Prestretch

To use the bistable actuator for transition between different locomotion modalities, the actuator needs to meet certain design and performance requirements. We start by investigating the influence of prestretch of the elastic membrane on the natural curvature of the actuator. The natural curvature is determined by assuming constant curvature along the 3D printed elastomeric frame and fitting the shape of the frame to a circular arc.

Three bistable actuators are fabricated at each prestretch (λ_p) of the elastic membrane ranging from 1.0 to 3.0. After fabricating the actuators (Figure S1, Supporting Information), they are activated five consecutive times to remove the Mullin's effect associated with the elastic membrane and left unactivated for 5 min. Then, the curvature is measured for all actuators.

Figure 2A shows the curvature as a function of the prestretch of the elastic membrane. It is observed that the natural curvature increases from 0.002 mm^{-1} to 0.060 mm^{-1} as the prestretch increases from 1.0 to 3.0. This results from the increasing elastic forces exerted by the elastic membrane with higher prestretch.

In the next subsections, we examine the influence of membrane prestretch on the geometric and blocking force properties of the actuators. This is accomplished through experimental characterization as well as analytic model and numerical simulation of the bistable actuators.

2.3. Analytic Model

We develop an analytic model based on the principle of minimum potential energy in order to better understand the underlying principle behind this bistable behavior. When there is no input voltage on the SMA, the total potential energy of the system (U_{total}) can be considered as the sum of the potential

energy of the prestretched membrane ($U_{membrane}$) and the frame (U_{frame}):

$$U_{total}(\theta,\lambda_p) = U_{membrane}(\theta,\lambda_p) + U_{frame}(\theta) \quad (1)$$

where λ_p is the prestretch of the membrane and θ is the bending angle of the bistable actuator. When the entire structure bends, U_{frame} will increase while $U_{membrane}$ will decrease. Due to the competition between these two contributions to potential energy, it is possible to reach an equilibrium point that minimizes U_{total}. For a prescribed initial prestretch (λ_p), this corresponds to the condition

$$\frac{\partial U_{total}}{\partial \theta} = 0 \quad (2)$$

The result of this analytic model is shown as the black solid line in Figure 2A, which exhibits good agreement with the experimental data on the stable state curvature of the bistable actuator. It should be noted that this is just one version of our analytic model that is based on the Yeoh hyperelastic model. We also adopt other hyperelastic models such as the Ogden and Mooney–Rivlin models, both of which also show reasonable agreement with the experimental data. Details of the derivation of the analytic model are included in the Supporting Information (Figures S2–S4, Supporting Information).

2.4. Numerical Simulation

Apart from the analytic model, which provides a macroscale understanding of the bending deformation, we also investigate numerical simulation to better study the internal mechanics of the bistable actuator (i.e., local stress and strain). By adopting the finite element method (FEM) simulation using ABAQUS (SIMULIA, Dassault Systémes), we capture the formation process of the stable state after releasing the actuator from prestretch (Movie S3, Supporting Information). Additionally, the simulation provides a detailed understanding of the actual shape of the actuator (see Figure S5A,C,E,G, Supporting Information) as well as the internal stress (see Figure S5B,D,F,H, Supporting Information) under various values of prestretch λ_p, respectively. By observing the local stress distribution, we notice that the stress on the membrane will concentrate more on its two ends under large prestretch, especially the four edges, which matches the major yielding position of the real actuator. A more detailed description of this numerical simulation can be seen in the Supporting Information.

2.5. Force Characterization

After investigating the influence of prestretch of the elastic membrane on the geometry of the actuator, we study its influence on force properties. Bistable actuators with prestretch <2.0 are not considered for the force measurements because they have very small curvature as observed by experimental and analytic studies. Also, analytic studies predicted no curvature with prestretch <1.9 (Figure 2A). First, we measure the "transition forces"—i.e., the mechanical force required to change from state I to state II and vice versa—required to surmount the energy barrier between the bistable states (without electrical input). This involves applying compression at 10 mm min^{-1} using a mechanical testing machine (Instron 5969) with 10 N load cell (inset Figure 2B; Figure S7A, Supporting Information). This is used to infer the maximum loading capability opposite to the bending direction of the bistable actuator while maintaining a steady state, which is important in the design of multimodal soft robots. There is an approximately fourfold increase in the transition force (from 0.27 to 0.94 N) as the prestretch increases from 2.0 to 2.8 (Figure 2B). The transition forces for prestretch (λ_p) of 2.6 and 2.8 are in similar range as shown in Figure 2B.

Next, we investigate the influence of membrane prestretch and operational conditions on the actuator's blocking force. The objective of the experiment is to infer how much payload the actuator can lift and flip to the other side. This is an important metric in designing soft robots with this bistable actuator. Such force is measured as a function of the membrane prestretch (λ_p) and operation parameters (i.e., voltage and activation time). We have limited the prestrech to the range of 2.4 to 2.8 for the blocking force measurements in order to provide the force and natural curvature that are appropriate for the robotic applications shown in Figure 1. Based on the results from preliminary experiments, actuators fabricated with a prestretch below 2.4 have small natural curvature and passive forces that are inadequate for robotics applications. Likewise, actuators fabricated with a prestretch of over 2.8 have a relatively high snap-through energy barrier and cannot transition to the other state when powered by a miniaturized LiPo battery (11.1 V). As shown in Figure S7B, the bistable actuator is fixed on a 3D printed jig and the distance between the actuator and the force plate is adjusted to make them just in contact. The force plate is fixed on a load cell (10 N) connected to the mechanical testing machine (Instron 5969) and the blocking force is registered as the actuator is activated at 11.1 V.

The bistable actuators fabricated with a pre-stretch of 2.4, 2.6, 2.8, and 3.0 are activated at 11.1 V for 50–300 ms at an interval of 50 ms, respectively. As shown in Figure 2C, there is a ninefold increase in blocking force (from 0.04 to 0.36 N) for actuators with a prestretch of 2.4, as the activation time is increased from 50 ms to 300 ms. The blocking force for the actuators with a prestrech of 2.6 and 2.8 is increased from ≈0.04 to ≈0.16 N and ≈0.04 to ≈0.11 N, respectively. With longer activation time, more of the Martensite phase within the SMA coil is transformed to the Austenite phase, leading to an increased contraction force. Since the force plate blocks the deformation of the actuator, the increased contraction force from the SMA coil results in an increased blocking force.

Figure 2D shows the blocking force of the bistable actuators activated under 11.1 V for 200 ms at both state I and II. As prestretch increases from 2.4 to 3.0, the antagonistic elastic forces from the elastic membrane are significantly increased and thus the blocking forces decrease from 0.18 to 0.08 N and 0.42 to 0.09 N at state I and state II, respectively. For the prestrech of

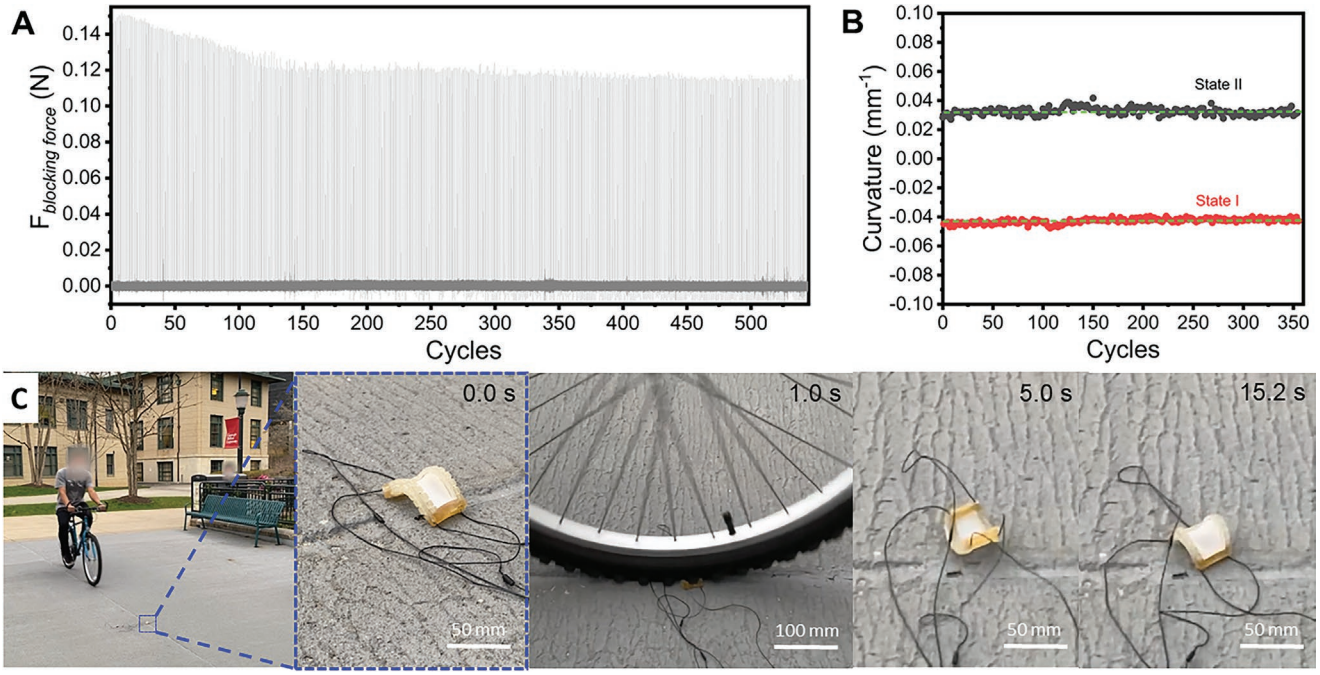

Figure 3. Cyclical activation and impact. A) Fatigue test, B) Cyclic curvature analysis and C) Robustness test of bistable actuator is performed by driving a bicycle over it followed by actuation in both the states (t_a = 200 ms and t_c = 10 s) for bistable actuator with prestretch (λ_p) of 2.8.

2.8 and 3.0, the forces generated at both states are similar and thus are ideal for the implementation of bistable actuators on multimodal soft robots. For a pre-stretch of 3.0, the forces are <0.1 N whereas for 2.8, the forces are ≈0.25–0.3 N.

2.6. Energy Characterization

To evaluate the ability of the actuator to perform mechanical work, a pendulum setup is used to estimate energy output. A ping-pong ball weighting ≈2.9 g is suspended from a wire (32 AWG, Magnet wire, Arcor). A bistable actuator with membrane prestretches of 1.0 and 2.8 are tested (Figure 2E; Movie S4, Supporting Information). Both bistable actuators are activated for 0.2 s at 11.1 V and measurements are performed to determine the corresponding velocity along x-axis, displacement along y-axis, and contact time. The displacement along the y-axis is 20.1 ± 3.0 mm (ΔH_1) and 26.2 ± 3.2 mm (ΔH_2), respectively, and thus the increase in ping-pong ball's gravitational potential energy is 0.57 ± 0.08 mJ and 0.75 ± 0.09 mJ, respectively, which corresponds to 30.9 ± 4.6% increase in potential energy transferred to the pendulum when increasing the membrane prestretch from 1.0 to 2.8. In contrast, increasing membrane prestretch decreases the duration of impact, with 67.1 ± 1.2 and 39.8 ± 4.6 ms contact times measured for λ_p = 1.0 and 2.8, respectively (Figure 2F; Figure S8A, Supporting Information). These experiments suggest that bistable actuators with 2.8 prestretch can generate larger displacements with lower contact time than the one with 1.0 prestretch, while the systems's input energy remains the same (Figure S8B, Supporting Information).

2.7. Cyclical Activation and Impact

To evaluate the response of the actuator to cyclical testing and impact, we limit our study to actuators with a membrane prestretch of 2.8. This value is chosen since these actuators exhibit the greatest force output and range of motion while also being responsive to electrical stimulation from an 11.1 V power source.

For the cyclical testing, the actuator is activated under 11.1 V with an activation time of 200 ms and a following cooling time of 30 s using the same experimental setup for 580 cycles (Figure S7B, Supporting information). The blocking force is about 0.15 N for initial cycles and then drops to 0.12 N after 125 cycles (**Figure 3**A). The force for the remaining cycles in the test are almost constant. Along with the fatigue test, cyclic activation test is performed for the curvature analysis. It is observed that the curvature remains constant even after 350 cycles on both states as seen in Figure 3B.

To test the robustness of the actuator, a rider (95.1 Kg) rides a bicycle (Huffy highland mountain bike, 16.0 Kg) over the bistable actuator causing it to be struck twice, i.e., once by front wheel and second time by rear wheel, respectively (Figure 3C; Movie S5, Supporting Information), After the strikes, the actuator is activated on both sides at an input of 11.1 V (t_a = 200 ms and t_c = 10 s) and is able to transform swiftly between two states (Figure 3C; Movie S5, Supporting Information). We also performed the compression test on the bistable actuator under different strain ranging from 70 to 90% using 50 kN load cell at 10 mm min^{-1} strain rate (Figure S9, Supporting Information). The actuator survives after 70 and 80% compression, corresponding to a compression load of 61 and 388 N. After 90%

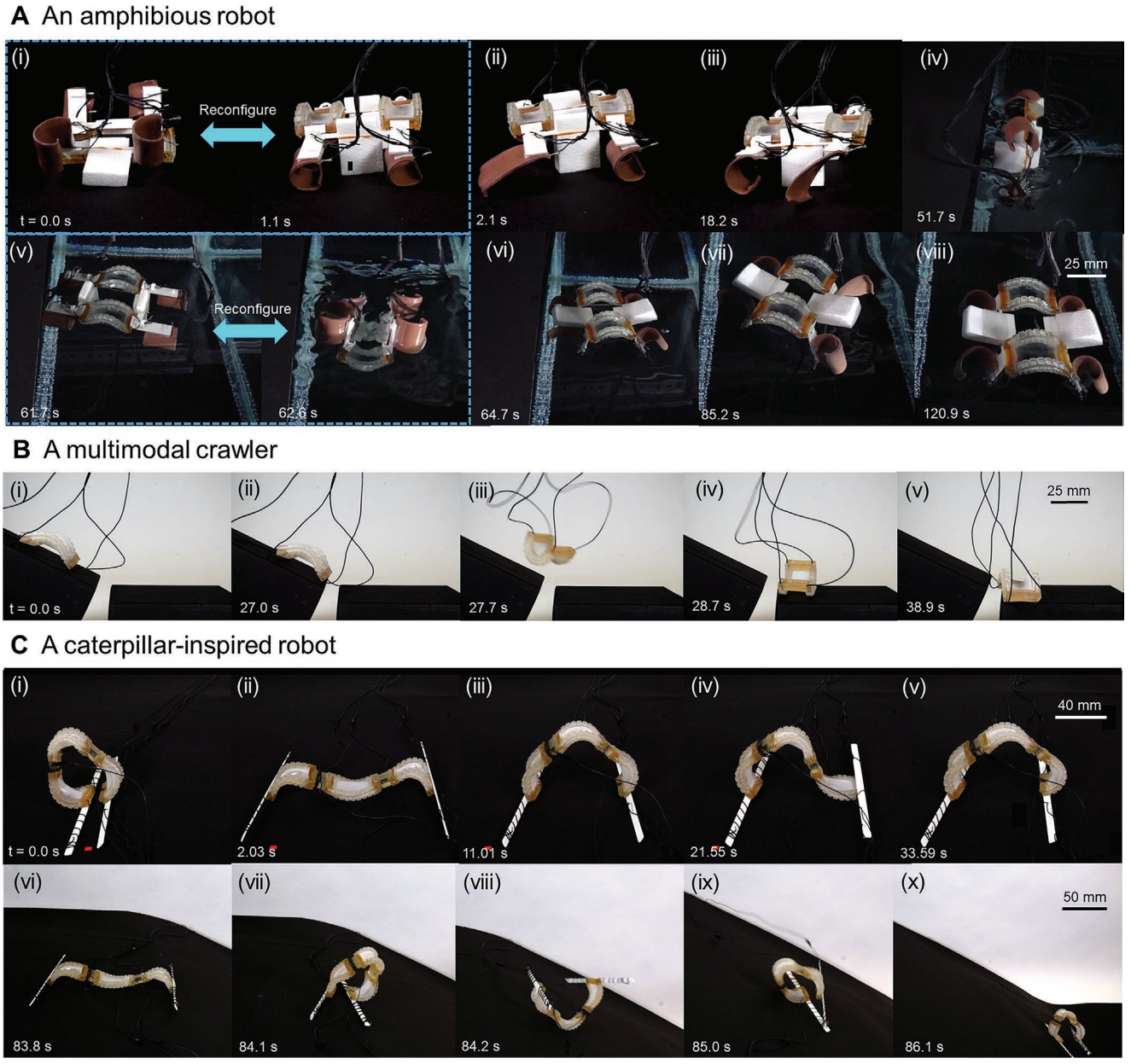

Figure 4. Reconfigurable amphibious and multimodal soft robots. A) An amphibious robot (i) reconfigure from swim mode to walk mode, (ii–v) walks toward the water reservoir along with dropping into it, (vi) reconfigures from walk mode to swim mode in water and (vii,viii) swims toward other side of reservoir (toward shore), B) A multimodal crawler (i–iii) crawls toward the cliff and (iv,v) jumping across the cliff followed by reconfiguration to crawl mode, and C) A caterpillar-inspired soft robot (i–v) shows crawling mode and (vi–x) rolling mode.

compression strain, corresponding to a compression load of 1039 N, the actuator can only undergo a few actuation cycles until one of the SMA springs pops out due to polymer failure (Movie S6, supporting information). This suggests that the bistable actuator is mechanically robust and can resist high dynamic loading and impact.

2.8. Multimodal Soft Robot Locomotion

This highly dynamic and compact bistable soft actuator is particularly enabling for fast actuation and multimodal locomotion for soft robots at centimeter scale. We demonstrate this by creating three shape-reconfigurable soft robots that are composed of the bistable actuators for actuation and transition between different modes of locomotion, including an amphibious soft robot and two multimodal soft robots.

2.8.1. An Amphibious Robot

Referring to Figure 1D and **Figure 4**A, the amphibious robot is composed of two bistable actuators with $\lambda_P = 2.8$ prestretch connected by two 3D printed C-shape connectors (PLA) and four

SMA-driven soft limbs.[31] The details of fabrication are included in the Supplementary Information. As the name suggests, the robot is capable of both crawling on land and swimming in water (Figure 1D). We use the bistable actuators as bridges to connect two pairs of SMA-driven soft limbs and take advantage of their bistability to transform between a quadruped crawler and a frog-like swimmer. Figure 4A(i) shows the swimmer-to-crawler transformation process of the amphibious robot on land. Both bistable actuators are curved upward in the swimming mode configuration. To transform to a crawler, the SMA coils in the lower frames (A1) of both bistable actuators are activated at 11.1 V for 200 ms. After the swimmer-to-crawler transition, the SMA-driven soft limbs of the robot are activated in a symmetric pattern[32] at 13.1 V (t_a= 200 ms and t_c = 2 s) to drive the robot approaching the pool (Figure 4A(ii,iii)). The robot continues to crawl until it falls into the pool (Figure 4A(iv,v)). Then we transform the robot from a crawler to a swimmer by activating the SMA coils in the top frame (A2) of both bistable actuators (Figure 4A(v)). Due to the buoyancy created by the foam, the robot makes a 180° flip (Figure 4A(vi)). Finally, the SMA limbs are activated in series with an activation time of 300 ms (t_a = 300 ms) and a subsequent cooling time of 1s (t_c = 1 s). This causes the robot to swim to the other side of the pool as demonstrated in Figure 4A(vii,viii) and Movie S7, Supporting Information. The amphibious robot travels in walking mode at 0.07 BL s^{-1} and in swimming mode at 0.06 BL s^{-1}. The control signal used for amphibious locomotion is shown in Figure S10 (Supporting Information).

2.8.2. A Multimodal Crawler

The second demonstration involves the use of a single bistable actuator fabricated with λ_P = 2.8 prestretch as both a crawler and a jumper. A gap in the ground terrain was created using two blocks separated by a distance of 12 mm (Figure 4B). As shown in Figure 4B, the robot crawls down the slope at 0.01 BL s^{-1} toward the gap by cyclically driving the SMA coil in the lower frame under 8.5 V (t_a = 200 ms and t_c = 10 s). The robot then falls into the gap with the same gait (Figure S11 and Movie S8, Supporting Information). To navigate the robot through the gap, we take advantage of the large energy change in the fast snap through activation process resulting in a jumping locomotion. As the robot approaches the gap, we enable the jumping locomotion by activating the SMA coil in the top frame of the actuator (A2, t_a = 200 ms and t_c = 10 s) at 13.5 V (Figure 4B(iv,v) and Movie S8, Supporting Information). By activating the SMA coil in the lower frame of the actuator A1, the robot can transform back to the crawler mode (Figure 4B(vi)) and continue crawling. The control signal used for multimodal crawler is shown in Figure S12 (Supporting Information).

2.8.3. A Reconfigurable Caterpillar-Inspired Robot

Lastly, we demonstrate a reconfigurable robot inspired by caterpillers that is capable of both crawling with a sinusoidal wave gait and curling its body to swiftly roll away. The robot is composed of three bistable actuators connected in series by two 3D printed connectors (epoxy aliphatic acrylate and urethane acrylated based elastomer) and two 3D printed (polylatic acid, PLA) beams attached at both ends of the robot to keep balance (see Figure 1E and Figure 4C). The robot can crawl on a flat surface by cyclically actuating the middle and front bistable actuators. The robot starts in an arc shape (Figure 4C(i)) and changes to a sinusoidal configuration (Figure 4C(ii)) by actuating the top frame of the middle actuator. It changes back to the arc shape by actuating the bottom frame of the middle actuator followed by front bistable actuator in outward and inwards direction. This results in the displacement of the crawling mode (Fig 4C(i–v)). This cycle is repeated, enabling the crawler to approach a declined portion of the ground terrain at 0.08 BL s^{-1} (Figure 4(vi)). To swiftly and efficiently navigate down the decline, we activate the SMA coil in the bottom frame of the middle actuator at 13.1 V for 200 ms. This causes the robot to curl into a closed arc and roll down the decline at 1.33 BL s^{-1} (Figure 4C(vi–x); Movie S9, Supporting Information). The control signal used for a reconfigurable caterpillar-inspired robot is shown in Figure S13 (Supporting Information).

3. Discussion and Conclusion

In this study, we develop a highly dynamic, robust, bistable soft actuator by sandwiching a prestreched elastic membrane between two 3D printed rectangular soft frames that are embedded with a pair of SMA coils. By taking advantage of both the bistability associated with the design and the fast response of the SMA, the actuator can reversibly transition between two oppositely curled configurations within 0.2 s when powered at 11.1 V. The observed maximum frequency of the actuator is 1 Hz (t_a = 0.1 s and t_c = 0.9 s) when no exterior loading is applied. In the experimental characterization and applications, we use longer t_a and t_c (i.e., t_a = 0.2 s and t_c = 10 s) to guarantee reliable actuation as well as consistent performance. Furthermore, the actuator is energetically stable at each state and can resist a maximum loading of 0.94 N without consuming energy (in the case of actuators with a membrane prestretch of 2.6 and 2.8). Lastly, the actuator exhibits a consistent response over repeated activation cycles and remains functional after high load impact from a bicycle.

The experimentally-observed actuator response is explained using a theoretical analysis based on the principle of minimum potential energy. The energy analysis accounts for the elastic strain energy of the prestretched membrane and the energy associated with the 3D printed frames. The model suggests a double-well potential energy profile that is consistent with the snap-through instability and bistable behavior that is empirically observed. Moreover, comparing predictions for the actuator bending curvature as a function of the membrane prestretch λ_p shows reasonable agreement between theory and experiment for a variety of hyperelastic constitutive models.

We show that the bistable actuator demonstrated here can be used to create shape-reconfigurable soft robots capable of multimodal locomotion. Specifically, we incorporate the actuators into an amphibious soft quadruped, a multimodal soft crawler, and a reconfigurable caterpillar-inspired soft robot. For these applications, the soft bistable actuator exhibits the following

enabling properties: i) relatively low requirement on power and control electronics; ii) ability to maintain various stable shapes without the need for continuous energy consumption; iii) rapid actuation for swift transition between different modes of locomotion. In contrast, past approaches that utilize thermal stiffness-tuning systems for mode transitions of amphibious robots require high energy consumption and have low shape morphing speed.[12] Compared to other soft bistable actuators, methods that utilize pneumatic-driven mechanisms[16,19,20,23] and dielectric elastomer[24] require bulky hardware for power and control. While untethered, soft bistable actuators that rely on the ambient environment (e.g., solvent[26] and temperature change[17]) for bistable actuation have limited applications. Compared with the SMA flexible bistable actuator presented in [18], the SMA soft bistable actuator in this work reduces the activation time and energy consumption by 90% (from 2 to 0.2 s) and 83.2% (from 25 to 4.2 J), respectively and improves the maximum activation frequency by 450% (from 0.182 to 1 Hz) (**Table 1**). Although the SMA flexible bistable actuator presented in [33] can generate larger force (3 N), this work improves the maximum activation frequency by 1105% (from 0.083 to 1 Hz) and 1654% (from 0.057 to 1 Hz), reduces energy consumption by 66.1% (from 12.4 to 4.2 J) and 91.3% (from 48 to 4.2 J), and reduces the activation time by 95.6% (from 4.5 to 0.2s) and 97.3% (from 7.5 to 0.2 s) when transformed from state I to state II and vice versa. (Table 1) Furthermore, the compactness, compliance, and robustness of the actuator are significantly improved by incorporating 3D printed frames (See Table 1).

The experimental characterization and robot demonstrations highlight the fast response, high force, light weight, compactness, and robustness of this SMA-driven bistable soft actuators. The bistable actuators consume more energy for periodic motions. However, the bistable actuation can also lead to faster response and higher force output that benefits fast periodic locomotion, as demonstrated by Tang et al.[16]

Beyond mobile soft robots, we foresee the potential application of this class of bistable soft actuators to other domains like wearable robotics, haptics, and shape-reconfigurable apertures for dynamically tunable communication. However, further studies will be required to investigate how the design principles explored here can be adapted for these applications. Of particular importance will be the regulation of heat for more rapid cooling of SMA coils and safe interaction with human skin and tissue.

4. Experimental Section

Fabrication of Bistable Actuator: A schematic of the fabrication process for bistables actuator is shown in Figure S1 (Supporting Information) and details are discussed below. First, 3D printed elastomeric hollow frames using a Digital light processing (DLP) based 3D printer (Asiga Pico2 HD) were used. The elastomeric resin used to print these frames comprised of epoxy aliphatic acrylate (49.02 wt.%), urethane acrylate (49.02 wt.%), and TPO (1.96 wt.%, Diphenyl(2,4,6-trimethylbenzoyl)phosphine oxide, Genocure TPO, RAHN USA Corp.) as photo initiator.[34,35] The printer is a top-down DLP system with a digital mirror device (DMD) and a UV–LED light source operating at 385 nm. The printer was maintained at 40 °C during printing and each layer was irradiated for 0.5 s and layer thickness was 100 µm. The detailed printing parameters are included Table S3 (Supporting Information). The printed structures were sonicated with

Table 1. Comparison of soft bistable actuators.

Actuator technology	Activation time T_{on} [s]	Resttime T_{off} [s]	Total time forsingle actuation T_{total} [s]	Voltage [V]	Current [A]	Input Pressure [kPa]	Energy consumption [J]	Efficiency	Bistable Actuation Without Human Interaction	Application	Reference
Pneumatic	0.09–0.1	0.04–0.23	0.13–0.15	Not provided	Not provided	20 - 30	Not provided	Not provided	Yes	Fast Soft Robot	[16]
Pneumatic	0.112	0.605	0.717	Not provided	Not provided	50	Not provided	Not provided	Yes	Soft Gripper	[21]
Pneumatic	0.101	0.069	0.17	Not provided	Not provided	106	Not provided	Not provided	Yes	Soft Gripper	[19]
Pneumatic	0.23–8	0.28 - 16	0.51–24	Not provided	Not provided	10/16	Not provided	Not provided	Yes	Soft Valve	[23]
DEA	≈3	≈1.5	≈4.5	≈5000–8000	Not provided	N/A	Not provided	Not provided	Yes	Soft Valve	[24]
Solvent	4	Not provided	Not provided	N/A	N/A	N/A	0	N/A	No	Soft Electronics	[26]
SMP (ambient temperature)	2.29	≈27.71	≈30	N/A	N/A	N/A	0	N/A	No	Mobile Soft Robot	[17]
Magnetic	≈0.05	≈0.95	≈0.1	N/A	N/A	N/A	0	N/A	Yes	Soft Electronics	[27]
SMA	2	3.5 - 8	5.5–10	5	2.5	N/A	25	Not provided	Yes	Fast Soft Robot	[18]
SMA	4.5–10	7.5	12–17.5	4.6–8	0.6	N/A	12.4–48	Not provided	Yes	Fast Soft Gripper	[33]
3D printing + SMA	0.1–0.2	0.9 - 10	1–10.2	≈8.7	≈2.4	N/A	≈4.2	0.16%–0.19%	Yes	Amphibious and Multimodal Soft Robot	This work

isopropyl alcohol (IPA) for 3 min to remove uncured resin followed by a 6 min post curing in a UV oven (UVP CL-1000 UV Oven). SMA coils (Flexinol spring, 30 coils, 0.203 mm diameter, Dynalloy Inc.) were stretched to four times the original length, inserted in the 3D hollow frames (Figure S1B, Supporting Information) and connected with the flexible wire. The end of wires were secured at one place using urethane adhesive (Ure-Bond II, Smooth-On). The VHB tape (4905, 3 M) was cut into rectangular sheets with a dimension of 55 mm × 90 mm × 0.5 mm using a CO_2 laser cutting system (30 W VLS 3.50; Universal Laser Systems). These sheets were prestretched from 1.0 to 3.0 using a linear stretcher (A150602-S1.5, Velmex) for ten times to remove any residual stresses or inelasticity associated with the Mullin's effect. The two elastomeric frames with embedded SMA springs were placed on the center of pre-stretched VHB tape on the top and bottom (Figure S1C, Supporting Information). This sandwich device was left 20 min for good bonding. The excess of the VHB tape was cut out along the outline of the 3D printed frames with embedded SMA with a pair of scissors (Figure S1D,E, Supporting Information).

Amphibious Robot: Two bistable actuators with 2.8 prestretch (λ_p) were used to fabricate the amphibious robot. They were connected in parallel using a 3D printed connector (PLA, Ultimaker S5) as shown in Figure 1D. The limbs were connected to the frames using velcro.

The limbs for the amphibious robot were fabricated using a method previously reported by Huang et al.[31] Two rectangular sheets of thermally conductive elastomer (dimensions: 55 mm× 22 mm × 0.5 mm and 70 mm× 37 mm× 0.5 mm H48-2, T-Global) were cut using a CO_2 laser cutting system (30W VLS 3.50; Universal Laser Systems). Next, a U shaped SMA wire (0.3 mm in diameter; resistance of 12.2 Ω m^{-1}, Dynalloy) was bend using a pliers with a dimension of 55 mm × 13 mm. The small rectangular thermal tape was coated with 0.2 mm-thick silicone elastomer. It was half cured at 50 °C for 7 min. U-shaped NiTi was placed on the smaller thermal tape with half cured silicone elastomer and another 0.4 mm-thick of uncured elastomer is applied over it and half-cured at 50 °C for 7 min. The larger thermal tape was stretched 60% strain for 10 times to remove any residual stresses or inelasticity associated with the Mullin's effect using a a linear stretcher (A150602-S1.5, Velmex). After applying 0.1 mm-thick uncured silicone elastomer on the larger prestretched thermal tape, the small thermal tape with half cured elastomer were clamped together using binder clips and placed in an oven at 50 °C for 10 min to fully cure it. A pair of scissors were used to cut along the line of the smaller thermal tape.

Multimodal Crawler: For the multimodal crawler, a single bistable actuator was used. For crawling motion, the lower frame (actuator A1) is activated at 8.5 V (t_a = 200 ms and t_c = 10 s). For jumping, the top frame (actuator A2) is activated at 13.5 V (t_a = 200 ms and t_c = 10 s).

Caterpillar-Inspired Soft Robot: Three bistable actuators were connected with 3D printed connector in the form of sinusoidal wave as seen in Figure 1E using Superglue (Loctite). Two PLA strips were attached to the end of the rolling bot. The dimension of the 3D printed (Ultimaker S5) strips were 5.75 mm × 145 mm. The angle for the slope is ≈27.85° to demonstrate the rolling motion.

Characterization: The natural curvature of the actuator (κ_n) was determined by assuming constant curvature and fitting the actuator shape to a circular arc as reported by [36, 37]. Rhino with the Grasshopper plugin as the computer-aided design software interface was used. Prior to this measurement, actuators were activated three consecutive times to eliminate any residual inelasticity associated with a "Mullins effect". Following each actuation signal for an activation time t_a = 0.2 s, the actuator remained unpowered for a cooling time t_c = 10 s during each cycle and was left for 5 min at room temperature before measurement.

Blocking force and fatigue tests were performed on an Instron 5969 Universal Testing Machine (10 N Load cell). For blocking force tests, a force plate was place above the bistable actuator to prevent motion as seen Figure S7B, Supporting Information. The actuator was then activated for various levels of the input, i.e., activation time, which is proportional to the total energy delivered. The cooling time (t_c) for the blocking force and fatigue test is 10 and 30 s, respectively.

Fatigue testing was performed using an almost identical physical setup to blocking force testing. The actuator was periodically activated with a 200 ms pulse every 30 s (i.e., cooling time t_c = 30 s) for over 600 cycles. These activation parameters were set to ensure that the actuator could fully cool before an additional actuation cycle to prevent thermal buildup.

Mechanical work using simple pendulum setup: A high-speed camera (Nova, Photron) at 5000 fps was used for this test. Video analysis was done using a tracking software (Image Systems, TEMA).

Supporting Information

Supporting Information is available from the Wiley Online Library or from the author.

Acknowledgements

D.K.P. and X.H. contributed equally to this work. The authors acknowledge support from the AFOSR Multidisciplinary University Research Initiative (FA9550-18- 1-0566; Program Manager: Dr. Ken Goretta) and the National Science Foundation Career Grant IIS2047912. The authors would also like to thank Rahn USA corporation for providing Genocure TPO and Allnex, USA for providing Ebecryl 113 (epoxy aliphatic acrylate, EAA) and Ebecryl 8413 (aliphatic urethane di-acrylate, AUD) samples. The authors would also like to thank Sathvik Divi to help for mechanical work setup using high speed camera. We would also like to thank Di Wu for helping in designing the cover art.

Conflict of Interest

The authors declare no conflict of interest.

Data Availability Statement

The data that support the findings of this study are available from the corresponding author upon reasonable request.

Keywords

3D printing, bistability, multimodal locomotion, shape memory alloy (SMA) powered

Received: August 2, 2022
Revised: October 11, 2022
Published online: November 18, 2022

[1] H.-T. Lin, G. G. Leisk, B. Trimmer, *Bioinspir. Biomim.* **2011**, *6*, 026007.
[2] B. Lindqvist, S. Karlsson, A. Koval, I. Tevetzidis, J. Haluška, C. Kanellakis, A. akbar Agha-mohammadi, G. Nikolakopoulos, *Robotics and Autonomous Systems* **2022**, *154*, 104134.
[3] Z. Wu, J. Liu, J. Yu, H. Fang, *IEEE/ASME Transactions on Mechatronics* **2017**, *22*, 2130.
[4] J. Yu, R. Ding, Q. Yang, M. Tan, J. Zhang, *Journal of Field Robotics* **2013**, *30*, 702.
[5] B. Zhong, S. Zhang, M. Xu, Y. Zhou, T. Fang, W. Li, *IEEE/ASME Transactions on Mechatronics* **2018**, *23*, 542.
[6] R. Baines, F. Fish, R. Kramer-Bottiglio, *Bioinspired Sensing, Actuation, and Control in Underwater Soft Robotic Systems,* **2021**, pp. 41–69, https://doi.org/10.1007/978-3-030-50476-2_3.

[7] R. Lock, S. Burgess, R. Vaidyanathan, *Bioinspir. Biomim.* **2013**, *9*, 011001.
[8] K. Low, T. Hu, S. Mohammed, J. Tangorra, M. Kovac, *Bioinspir. Biomim.* **2015**, *10*, 020301.
[9] T. F. Nygaard, C. P. Martin, J. Torresen, K. Glette, D. Howard, *Nature Machine Intelligence* **2021**, *3*, 410.
[10] S. Zhang, Y. Zhou, M. Xu, X. Liang, J. Liu, J. Yang, *IEEE/ASME Transactions on Mechatronics* **2015**, *21*, 1720.
[11] X. Liang, M. Xu, L. Xu, P. Liu, X. Ren, Z. Kong, J. Yang, S. Zhang, in *2012 IEEE/RSJ International Conference on Intelligent Robots and Systems*, IEEE, Vilamoura, Algarve, Portugal **2012**, pp. 3667–3672.
[12] R. L. Baines, J. W. Booth, F. E. Fish, R. Kramer-Bottiglio, in *2019 2nd IEEE International Conference on Soft Robotics (RoboSoft)*, IEEE, Seoul, Korea **2019**, pp. 704–710.
[13] D. S. Shah, J. P. Powers, L. G. Tilton, S. Kriegman, J. Bongard, R. Kramer-Bottiglio, *Nature Machine Intelligence* **2021**, *3*, 51.
[14] Y. Cao, M. Derakhshani, Y. Fang, G. Huang, C. Cao, *Adv. Funct. Mater.* **2021**, *31*, 2106231.
[15] Y. Chi, Y. Li, Y. Zhao, Y. Hong, Y. Tang, J. Yin, *Adv. Mater.* **2022**, *34*, 2110384.
[16] Y. Tang, Y. Chi, J. Sun, T.-H. Huang, O. H. Maghsoudi, A. Spence, J. Zhao, H. Su, J. Yin, *Sci. Adv.* **2020**, *6*, eaaz6912.
[17] T. Chen, O. R. Bilal, K. Shea, C. Daraio, *Proc. Natl. Acad. Sci. USA* **2018**, *115*, 5698.
[18] S. Nishikawa, Y. Arai, R. Niiyama, Y. Kuniyoshi, *IEEE Robotics and Automation Letters* **2018**, *3*, 1018.
[19] X. Wang, H. Zhou, H. Kang, W. Au, C. Chen, *Smart Mater. Struct.* **2021**, *30*, 125001.
[20] J. A. Faber, J. P. Udani, K. S. Riley, A. R. Studart, A. F. Arrieta, *Adv. Sci.* **2020**, *7*, 2001955.
[21] X. Wang, A. Khara, C. Chen, *Bioinspir. Biomim.* **2020**, *15*, 56017.
[22] F. Welsch, S.-M. Kirsch, P. Motzki, M. Schmidt, S. Seelecke, in *Smart Materials, Adaptive Structures and Intelligent Systems*, vol. *51944*, American Society of Mechanical Engineers, San Antonio, TX, USA **2018**, p. V001T04A014.
[23] P. Rothemund, A. Ainla, L. Belding, D. J. Preston, S. Kurihara, Z. Suo, G. M. Whitesides, *Sci. Rob.* **2018**, *3*, 16.
[24] S. Wei, T. K. Ghosh, *Soft Robotics* **2021**, *9*, 1.
[25] C. Megnin, J. Barth, M. Kohl, *Sens. Actuators, A* **2012**, *188*, 285.
[26] Z. Chen, S. Kong, Y. He, S. Yi, G. Liu, Z. Mao, M. Huo, C. H. Chan, J. Lu, *ACS Appl. Mater. Interfaces* **2021**, *13*, 41968.
[27] V. Ramachandran, M. D. Bartlett, J. Wissman, C. Majidi, *Extreme Mechanics Letters* **2016**, *9*, 282.
[28] X. Huang, M. Ford, Z. J. Patterson, M. Zarepoor, C. Pan, C. Majidi, *J. Mater. Chem. B* **2020**, *8*, 4539.
[29] Z. J. Patterson, D. K. Patel, S. Bergbreiter, L. Yao, C. Majidi, *Soft Robotics* **2022**, *0*, 1.
[30] X. Huang, K. Kumar, M. K. Jawed, A. M. Nasab, Z. Ye, W. Shan, C. Majidi, *Sci. Rob.* **2018**, *3*, eaau7557.
[31] X. Huang, K. Kumar, M. K. Jawed, A. Mohammadi Nasab, Z. Ye, W. Shan, C. Majidi, *Adv. Mater. Technol.* **2019**, *4*, 1800540.
[32] X. Huang, K. Kumar, M. K. Jawed, Z. Ye, C. Majidi, *IEEE Robotics and Automation Letters* **2019**, *4*, 2415.
[33] S.-W. Kim, J.-S. Koh, J.-G. Lee, J. Ryu, M. Cho, K.-J. Cho, *Bioinspir. Biomim.* **2014**, *9*, 036004.
[34] D. K. Patel, A. H. Sakhaei, M. Layani, B. Zhang, Q. Ge, S. Magdassi, *Adv. Mater.* **2017**, *29*, 1606000.
[35] M. Zadan, D. K. Patel, A. P. Sabelhaus, J. Liao, A. Wertz, L. Yao, C. Majidi, *Adv. Mater.* **2022**, *34*, 2200857.
[36] W. Wang, L. Yao, C.-Y. Cheng, T. Zhang, H. Atsumi, L. Wang, G. Wang, O. Anilionyte, H. Steiner, J. Ou, K. Zhou, C. Wawrousek, K. Petrecca, A. M. Belcher, R. Karnik, X. Zhao, D. I. C. Wang, H. Ishii, *Sci. Adv.* **2017**, *3*, e1601984.
[37] Y. Tao, Y.-C. Lee, H. Liu, X. Zhang, J. Cui, C. Mondoa, M. Babaei, J. Santillan, G. Wang, D. Luo, D. Liu, H. Yang, Y. Do, L. Sun, W. Wang, T. Zhang, L. Yao, *Sci. Adv.* **2021**, *7*, eabf4098.